Journal of Nuclear Materials 543 (2021) 152546

Contents lists available at ScienceDirect

Journal of Nuclear Materials

journal homepage: www.elsevier.com/locate/jnucmat

Effects of stress triaxiality and strain rate on the fracture of a CuCrZr alloy

Yiqiang Wang[a,*], Omar Mohamed[b], Keren Dunn[b], Tan Sui[b,*], Mutaz Bashir[a], Peter Cooper[a], Adomas Lukenskas[a], Guiyi Wu[c], Michael Gorley[a]

[a] Culham Centre for Fusion Energy, UK Atomic Energy Authority, Abingdon, Oxon, OX14 3DB, United Kingdom
[b] Department of Mechanical Engineering Sciences, University of Surrey, Guildford, Surrey, GU2 7XH, United Kingdom
[c] TWI Ltd., Great Abington, United Kingdom

ARTICLE INFO

Article history:
Received 19 May 2020
Revised 3 September 2020
Accepted 19 September 2020
Available online 24 September 2020

Keywords:
CuCrZr
Stress triaxiality
Loading-up strain rate sensitivity
Exhaustion of ductility
DDC-IC

ABSTRACT

Precipitation hardened Copper-Chromium-Zirconium (CuCrZr) alloy is a prime candidate for divertor components in future European DEMOnstration (DEMO) fusion reactors. To develop the DEMO Design Criteria for In-vessel Components (DDC-IC), the failure criterion of CuCrZr needs to be investigated. Hence, the effects of stress triaxiality and loading strain rate on the fracture of solution heat treated and annealed CuCrZr alloys were studied using digital-imaging-correlation and electron microscopy techniques. It was found that an increase in the stress triaxiality caused a significant decrease of over 50% in the equivalent strain to fracture. On the other hand, increasing applied strain rate from 1.3×10^{-5} $s^{-1}$to 8.6×10^{-3} s^{-1} had no considerable effects on the yield stress and elongation. However, higher flow stresses and a larger number density of voids were observed under the highest applied strain rate of 8.6×10^{-3} s^{-1}. Fracture surface analysis showed that the failure model was dominated by void growth and coalescence for all the tests. This work has been performed within the Engineering Data and Design Integration (EDDI) subproject of the EUROfusion Materials work package and aimed to contribute to the development of the DEMO Design Criteria for In-vessel Components.

1. Introduction

Copper-Chromium-Zirconium (CuCrZr) has been used as a structural heat sink material for water-cooled plasma-facing-components for over two decades in JET [1]. It has also been selected in ITER type water-cooled divertors and is the promising candidate material for divertor components in European DEMOnstration fusion power plants (DEMO, Fig. 1a), as shown in Fig. 1b-c [2–4]. When manufacturing the divertor, CuCrZr cooling pipes need to be joined to tungsten armour via brazing, hipping or other techniques (Fig. 1d). For brazing, it involves melting and flowing a filler metal (as shown in blue colour in Fig. 1d) into the joint of two metal items.

The divertor components are cooled using pressurised water and operate in extreme environments including high temperature, irradiation and cyclic multi-axial thermal and mechanical loads [5,6]. To develop the DEMO Design Criteria for In-vessel Components (DDC-IC), the development of the CuCrZr material property handbook (MPH) is also required [7]. Therefore, investigating the fracture behaviour of CuCrZr under monotonic loading conditions is required to support the fusion component design and to meet fitness-for-service criteria.

Ductility represents the ability of a material to withstand large plastic deformations prior to failure by fracture. Equivalent strain to fracture, $\bar{\varepsilon}_f$, is often used to represent the ductility of materials. The $\bar{\varepsilon}_f$ is given by

$$\bar{\varepsilon}_f = In\left(\frac{A_0}{A}\right) = 2In\left(\frac{r_0}{r}\right) \quad (1)$$

where r_0 and r are the initial and final (fractured) radii of the initial (A_0) and final (A) minimum cross-section of a round bar specimen.

For ductile materials, failure is often related to coalescence of microscopic voids. Over the last half century, a significant amount of work has been performed and has demonstrated that stress triaxiality (η) can influence the behaviour of void coalescence and reduce the equivalent strain to fracture [8–14]. The stress triaxiality is defined as

$$\eta = \frac{\sigma_H}{\bar{\sigma}} \quad (2)$$

* Corresponding authors.
E-mail addresses: yiqiang.wang@ukaea.uk (Y. Wang), t.sui@surrey.ac.uk (T. Sui).

https://doi.org/10.1016/j.jnucmat.2020.152546
0022-3115/

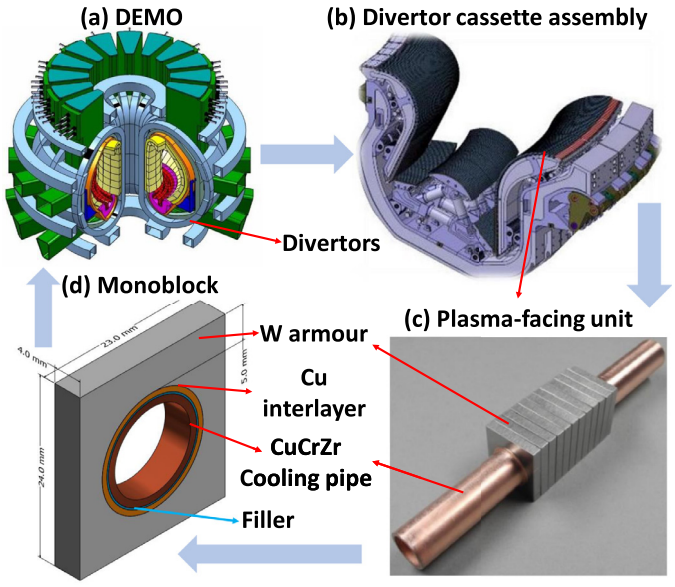

Fig. 1. (a) A schematic picture of a Europe Demonstration fusion reactor. Reprinted from [2], copyright © 2015 Institute of Materials, Minerals and Mining. (b) divertor cassette assembly and (c) a plasma-facing unit (reprinted from [3], with permission from Elsevier.) which consists of (d) tungsten armours brazing joined via an interlayer material to a CuCrZr cooling pipe.

where σ_H and $\bar{\sigma}$ are hydrostatic stress and equivalent stress given by

$$\sigma_H = \frac{\sigma_1 + \sigma_2 + \sigma_3}{3} \tag{3}$$

and

$$\bar{\sigma} = \sqrt{(\sigma_1 - \sigma_2)^2 + (\sigma_2 - \sigma_3)^2 + (\sigma_3 - \sigma_1)^2}/\sqrt{2} \tag{4}$$

where σ_1, σ_2 and σ_3 are principal stresses in decreasing magnitude.

Early work conducted by Johnson and Cook [10] and Mirsa and Barton [11] found that the ductility of a wide range of materials (OFHC copper, steel, pure iron and aluminium alloys etc.) decreases with the increase of stress triaxiality. Bao and Wierzbicki [12] indicated that for a 2024-T351 aluminium alloy, the fracture is governed by shear and void growth model with negative and large (>1/3) stress triaxialities respectively. When the values of stress triaxiality are in between 0 and 1/3, the combination of shear and void growth causes the fracture. Noell et al. [15] indicated that for a given stress state and material, up to seven different mechanisms can be associated in a sequential manner contributing to the failure of the material. These mechanisms can be a combination of void growth and coalescence, shear localization and the Orowan Alternating Slip (OAS) mechanisms etc. This is further confirmed by Croom et al. [16] who investigated the rupture process of a pure Cu wire using In situ X-ray computed tomography technique. It showed that a sequence of mechanisms started from shear localization, then to the voids growth and coalescence, and growth of the coalesced voids via OAS caused to the damage in the Cu wires.

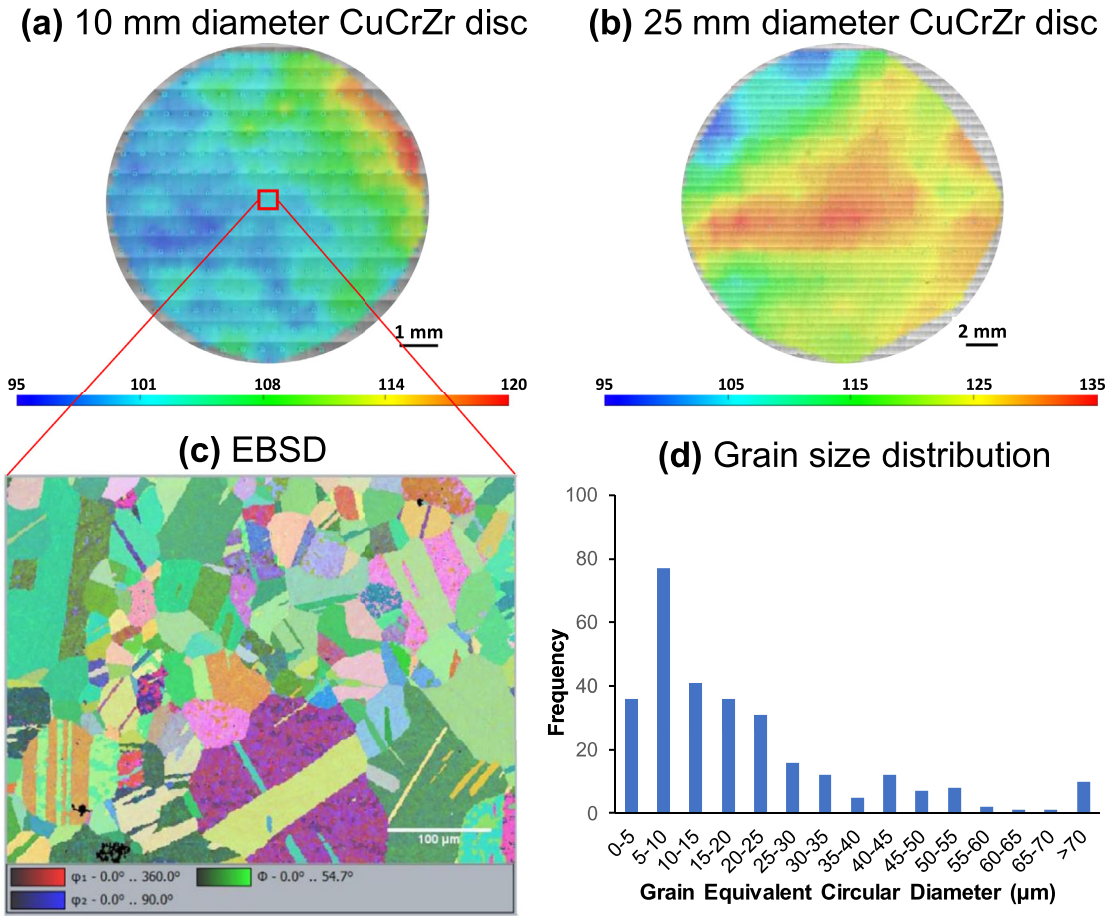

Fig. 2. Two-dimensional Vickers hardness mapping the cross sections of the heat treated (a) 10 mm and (b) 25 mm diameter CuCrZr rods. Microstructure characterisation of the heat treated CuCrZr alloy (c) Electron backscattered diffraction (EBSD) image showing the grain morphology, orientation and size and (d) grain size distribution from the centre of CuCrZr specimen

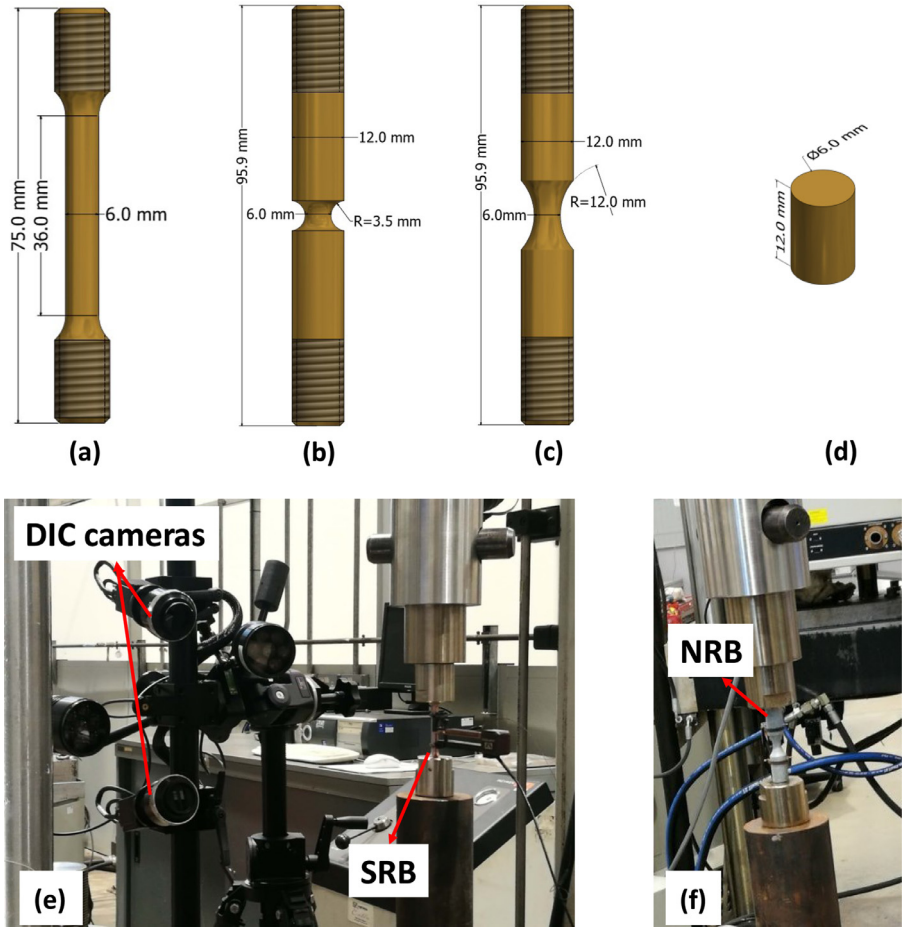

Fig. 3. CuCrZr specimen geometries for (a) smooth round bar (SRB) for uniaxial tension and torsion tests, (b and c) notched round bar (NRB) for uniaxial tensile and (d) cylinder for compression tests. (e) 3D-DIC set-up on the smooth round bar specimen and (f) a close view of a notched round bar specimen.

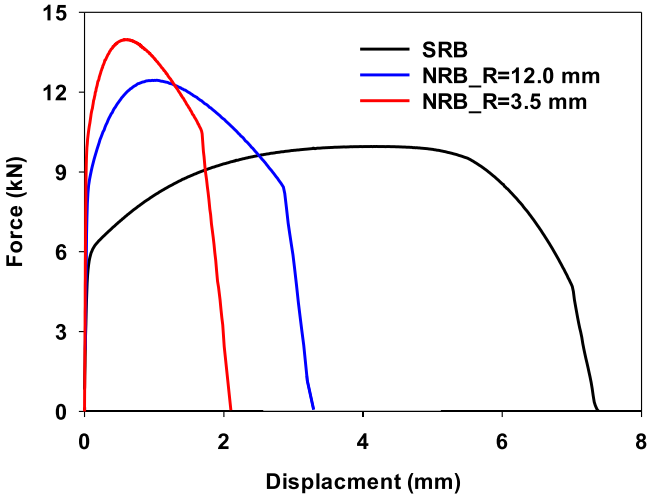

Fig. 4. Experimental force versus displacement along 25 mm gauge length curves for smooth round bar and notched round bars with notch radii of 12.0 mm and 3.5 mm respectively.

In these studies, the same loading displacement rate was often used to test specimens with and without notches. This brings the applied strain rate in the localised region of a notch bar specimen up to 35 times faster than that in a smooth round bar specimen. For a given material, since ductility depends on both stress triaxiality and loading strain rate, the decrease of ductility in notched bar specimens is suggested to be due to the combination effect of stress triaxiality and high loading strain rate [10,17–23]. Rao et al. [20] carried out tensile testing of CuCrZrTi alloy under loading strain rates ranging from 10^{-4} s^{-1} to 10^{-3} s^{-1}at both room and elevated temperatures. The results indicated that the yield strength and ultimate tensile strength increased with increasing strain at room temperature, but no changes in elongation and reduction in area were observed. Mirsa and Barton [11] also found that increasing the strain rate from 10^{-4} s^{-1} to 10^{-3} s^{-1} has no considerable effect on the fracture strain of pure iron and aluminium alloy bs1474. Wang et al. [22,23] indicated that both a larger positive stress triaxiality or a higher strain rate can promote the embrittlement of Ti6Al4V. However, the fracture mechanisms of Ti6Al4V is independent of the strain rate when the stress triaxiality is very high (0.5) or very low (−0.31).

To the best of the authors knowledge, only limited studies have been performed to investigate the effect of stress triaxiality and loading strain rate on the fracture failure of the current CuCrZr alloy. This study aims to decouple the effect of stress triaxiality and loading strain rate on fracture ductility of a heat treated CuCrZr alloy. Tensile tests on smooth round bar and notched round bar specimens were conducted in combination with digital-imaging-correlation (DIC) technique. Tensile tests on smooth round bars under different applied loading strain rates were also performed. Fracture surfaces were characterised using scanning electron mi-

Table 1
Summary of Tests ID, specimen dimensions, test type and initial value of stress triaxiality for each test.

Test ID	Specimen type	Test type	Gauge diameter/ length (mm)	Notch radius (mm)	Initial stress triaxiality
1–2	SRB	Tension	6/35	N/A	0.33
3–4	NRB		6/35	12	0.45
5–6	NRB		6/35	3.5	0.69
7–8	Cylinder	Compression	6/13	N/A	−0.2

Table 2
Summary of tests ID and applied loading strain rate for each test.

Test ID	Specimen type	Test type	Gauge diameter/ length (mm)	Loading-up strain rate (s^{-1})
9–10	SRB	Tension	6/35	1.3×10^{-5}
11–12		Tension	6/35	2.5×10^{-4}
13–14		Tension	6/35	8.6×10^{-3}

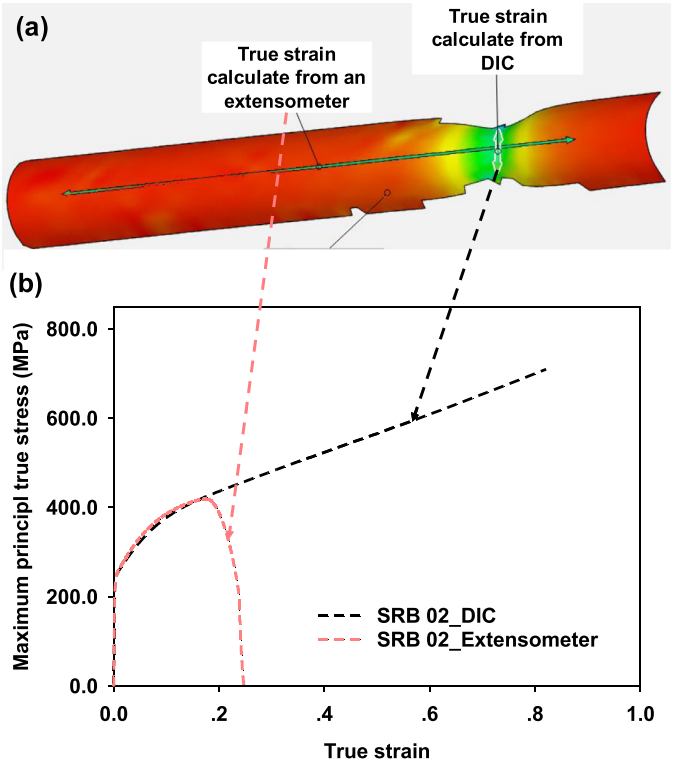

Fig. 5. (a) A DIC image shows necking region before fracture of the tensile Test (ID1) and (b) comparison of the true stress-strain plots derived from 25 mm gauge length along the loading direction and from the minimum cross-sectional area in the necking zone. It should be noted that the maximum principle stress is the stress along applied load direction.

croscopy (SEM) technique. Both macroscopic tensile fracture characteristics and underlying microscopic damage mechanisms in a CuCrZr alloy are presented in this paper.

2. Materials and microstructure characterisation

Commercial CuCrZr rods of 25 mm and 10 mm diameters and 100 mm lengths were used in the current study. The chemical compositions of the 10 mm and 25 mm CuCrZr rods are Cu-0.84Cr-0.08Zr and Cu-0.7Cr-0.13Zr (all in wt.%) respectively. Both materials meet the requirements of the ITER grade CuCrZr composition (0.6–0.9Cr% and 0.07–0.15Zr%, all in wt%) [6]. It is well-known that the mechanical properties of CuCrZr are significantly affected by thermo-mechanical processes [7,24]. To replicate the initial condition of the divertor component, these 100 mm long rods were heat treated in two-stages representing the brazing process as detailed in [25]. This involves solution heat treatment of the materials at 1020 °C for 2 min to dissolve the Cr and Zr into the Cu matrix, followed by annealing at 475 °C for 2 h to promote the formation of nanoprecipitates which provides optimised strength.

The microhardness (Hv) of cross sections of the heat treated CuCrZr rods with diameters of 10 mm and 25 mm were measured using a LECO microhardness tester with a load of 0.3kgf and a dwell time of 10 s. Samples were sectioned using the electrical discharge machining method, and grinded and polished by the normal methods. Fig. 2a and b show that the Vickers hardness mapping for the samples and the hardness values of 25 mm sample is ~20% greater (and less uniform) than those measured in the 10 mm diameter sample. This is thought to be due to the slight difference in chemical compositions between these two batches of CuCrZr and/or because of the relatively short amount of solution heat treatment time (2 min). Extra care is therefore necessary for this brazing process to produce fusion components with optimal and uniform mechanical properties.

The microstructure of the heat treated CuCrZr was characterised by a JSM-7100F field emission scanning electron microscope (FE-SEM) with a Thermo Fisher Scientific Lumis EBSD detector [26]. Samples were prepared using a standard method. Fig. 2c shows a face-centred cubic (FCC) Euler orientation image collected from the central region of a 10 mm diameter sample. The equivalent circular diameter (ECD) of grains were calculated from the equation $ECD = \sqrt{4A\pi}$ and using ImageJ software [27], where A is the area of the fitted oval (μm^2). Fig. 2d shows the grain size distribution histogram of a total 295 grains. The average grain size is approximately 25 μm ± 5 μm and over 25% of grains fall in the EDC range of 5 to 10 μm.

3. Experimental method

3.1. Tests with different stress triaxialities

Eight tests (as summarised in Table 1) including tensile tests for smooth round bar (SRB) and notched round bar (NRB) specimens, and compression tests for cylinder specimens on the CuCrZr alloy were performed to study the dependence of fracture ductility on stress triaxiality. These SRB, NRB and cylinder specimens, as shown in Fig. 3a–d, were designed to obtain four different initial stress triaxialities ranging from −0.2 to 0.7. The relationship between the value of stress triaxiality and the radius of notch, R, can be described by Bridgman equation below and given in [8]

$$\eta = \frac{1}{3} + In\left(\frac{r}{2R} + 1\right) \tag{5}$$

To ensure that the results are comparable, all the specimens for stress triaxiality study were manufactured using the 25 mm di-

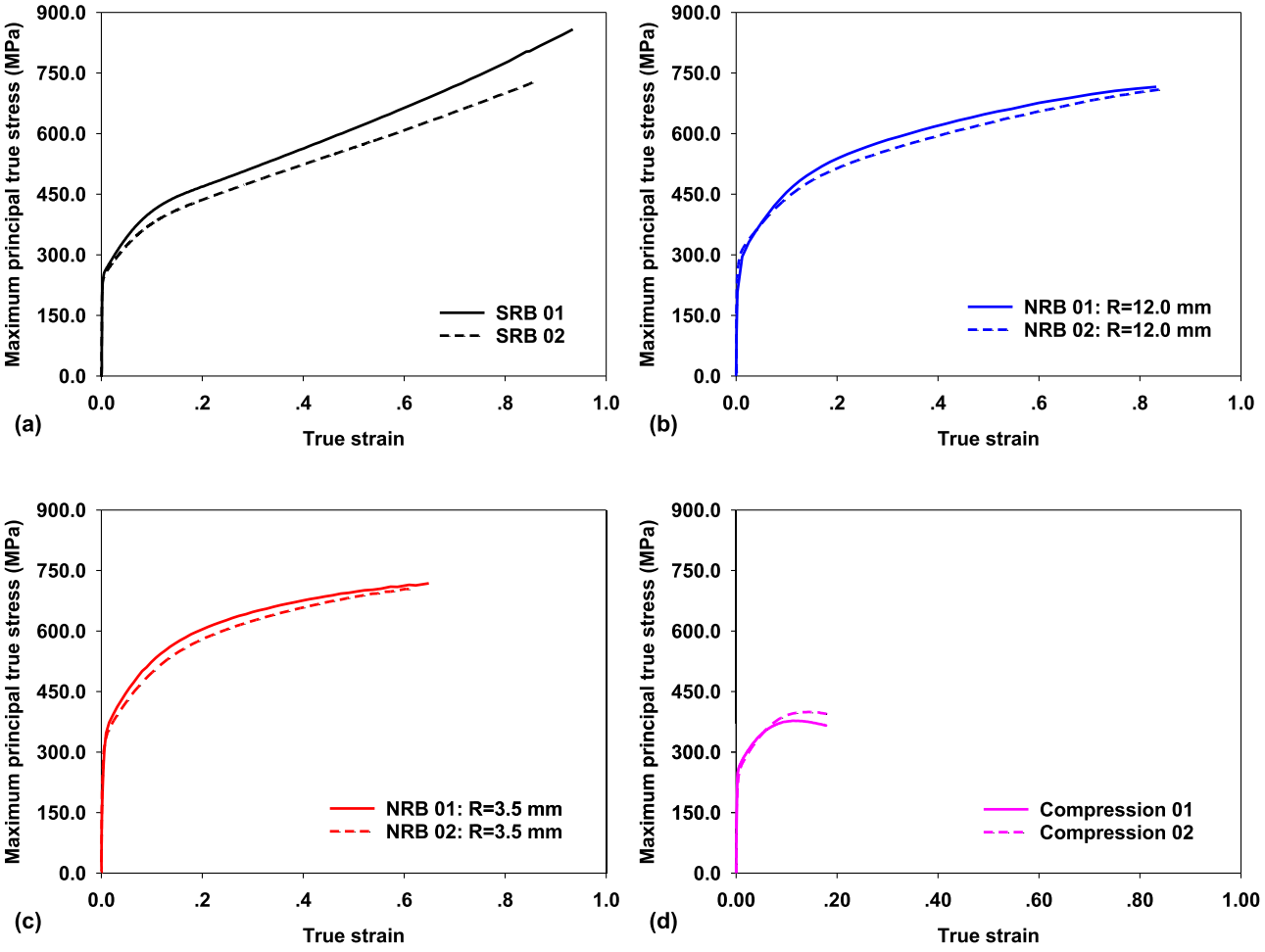

Fig. 6. The maximum principal true stress versus true strain plots for uniaxial tensile tests of CuCrZr (a) smooth round bar; notched round bar with notch radius of (b) 12 mm, (c) 3.5 mm and (d) compression tests using cylinder specimens.

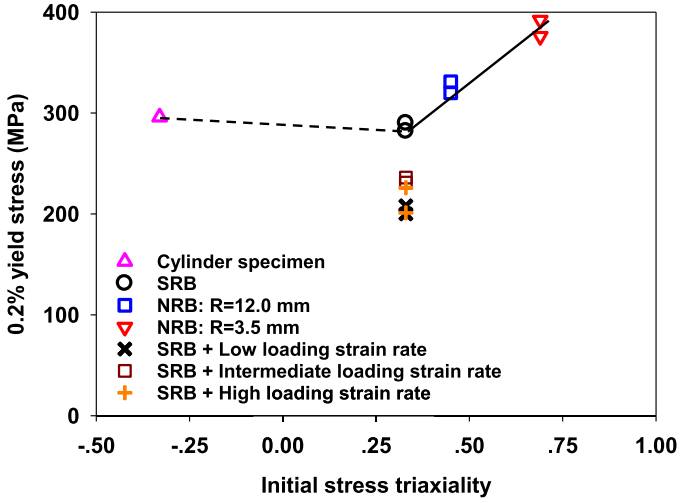

Fig. 7. 0.2% yield stress obtained from tests conducted at different stress triaxiality and applied loading strain rates.

ameter rods where the specimens for strain rate sensitivity study were manufactured from the 10 mm diameter rods.

These tests were performed using an INSTRON 8502 testing machine at an applied loading displacement rate of ~0.00875 mm/s. This gives an approximate applied loading strain rate of 2.5×10^{-4} s^{-1}along the gauge length of the smooth round bar specimen.

An extensometer with a 25 mm gauge length was used to measure the displacement change in the specimen's gauge length. True stress and strain measurements were also obtained using 3D stereoscopic DIC using a subset size of 35 pixels and a step size of 9 pixels, as shown in the set-up in Fig. 3e and f. Two samples were tested for each condition. Accurate equivalent fracture strains were not able to obtained from DIC due to the speckle pattern were in poor quality before failure.

3.2. Tests under different strain rates

The tensile testing for the strain rate sensitivity study was conducted using an Instron 5500R testing equipment [28], as summarised in Table 2. The displacement change across the specimen's gauge length was measured by a dynamic extensometer with 25 mm gauge length. A set of tests were carried out at applied loading displacement rates of ~0.025 mm/min, 0.5 mm/min, and 18.0 mm/min respectively. These loading displacement rates give applied strain rates of 1.3×10^{-5} s^{-1} (low), 2.5×10^{-4} s^{-1} (intermediate and standard) and 8.6×10^{-3} s^{-1} (high) in the gauge length of the smooth round bar specimen. The low and high applied strain rates are 1/20 and 30 times of the standard (intermediate) one, respectively. This set of tests was repeated once. The experimental set up for both stress triaxiality and strain rate stud-

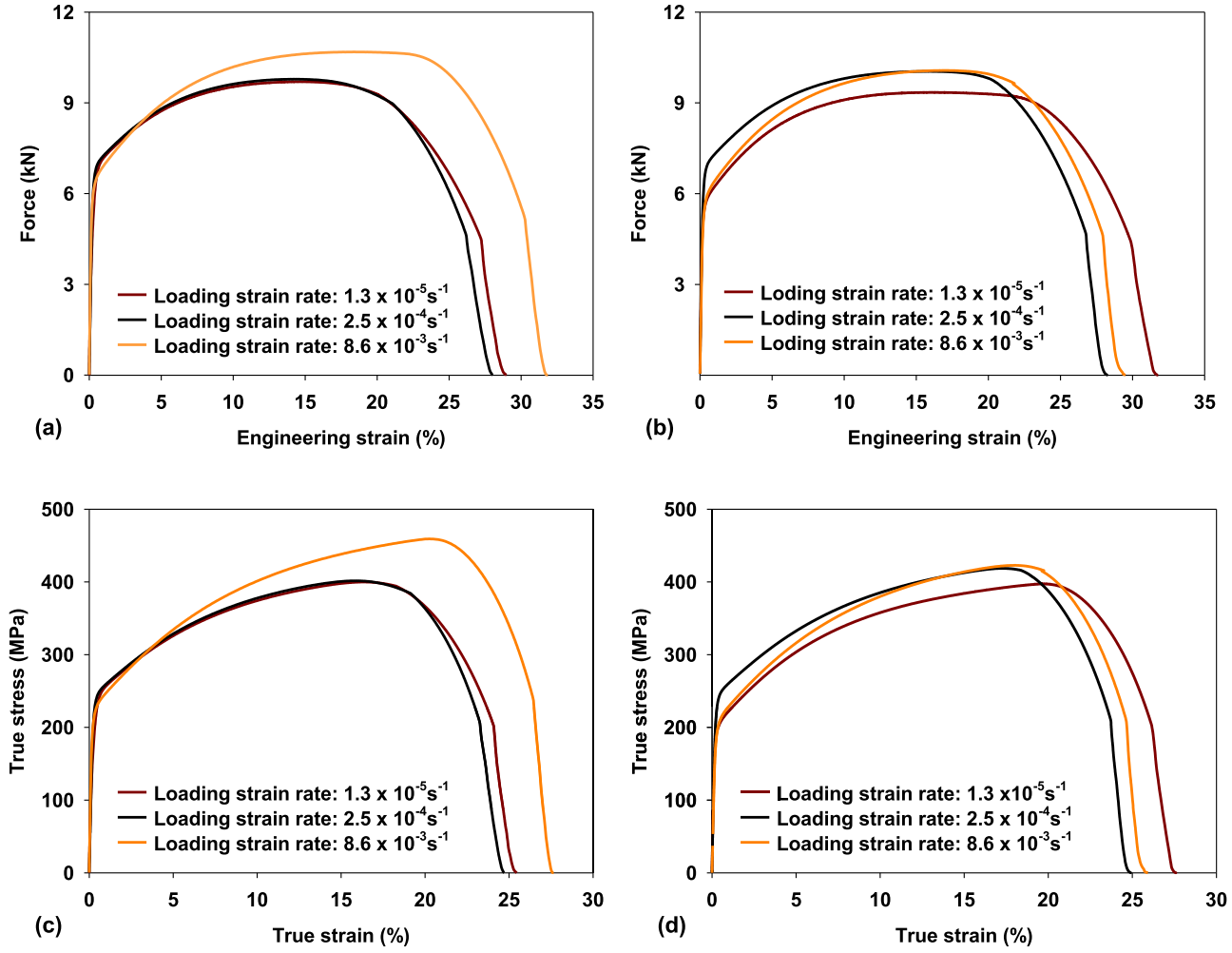

Fig. 8. (a-b) Force versus engineering strain plots and (c-d) true stress versus strain plots at different applied strain rates. (a and c) The first set of tests and (b and d) the second set of tests.

ies are in accordance to the respective ASTM, E8–99 tensile testing standards [29].

3.3. Fracture surface characterisation

Fracture features of failed tensile samples were characterised using SEM via a HITACHI 2–3200 N machine, a TESCAN Mira3 XHM and a JSM-7100F FE-SEM operated at a voltage of 20 kV [26]. SEM images were used to measure the diameter of the fractured surface which can provide more accurate measurements than using a micrometre. SEM images were further used to analyse the number density of the nucleated voids in the ductile failure zone further using ImageJ software. Four SEM images covering a total area of $400\mu m^2$ were analysed for each testing condition to provide quantitative results. These SEM images were acquired from four different regions at the central ductile fracture zone.

4. Experimental results

4.1. Tests with different stress triaxiality

The force-displacement curves for the SRB and two NRB specimens are shown in Fig. 4. The peak force increased approximately 20% and 10% with increased initial stress triaxiality from 0.33 to 0.45 and from 0.45 to 0.69 respectively. A similar trend is also observed for the force at yield. The displacement at failure decreased significantly with the increase of stress triaxiality. In order to obtain the maximum principal true stress with true strain across the necking zone, displacements perpendicular to the loading direction in the necking zone were calculated from DIC data for each test. The true strain (ε_t) and true stress (σ_t) were calculated from the equations in below.

$$\varepsilon_t = In\left(\frac{A_0}{A}\right) \tag{6}$$

$$\sigma_t = \frac{F}{A} \tag{7}$$

where F is the applied force; A_0 and final A are the initial and current minimum cross-section of the specimens.

A ~4 mm long digital strain gauge was used for tracking the diameter changes in the necking zone perpendicular to the loading direction, as shown in Fig. 5a. The maximum principal true stress with true strain plots of the uniaxial tensile test ID1 obtained from 25 mm gauge length along the loading direction (rose dash line) and the minimum cross sectional area in the necking zone (dark dash line) are shown in Fig. 5b. Clearly, the true stress-strain plots obtained from these two different methods are similar before necking, but significantly dissimilar after necking.

Fig. 6a–c show the maximum principal true stresses with true strain plots for uniaxial tensile tests of smooth round bar, notched round bars with notch radii of 12 mm and 3.5 mm, respectively.

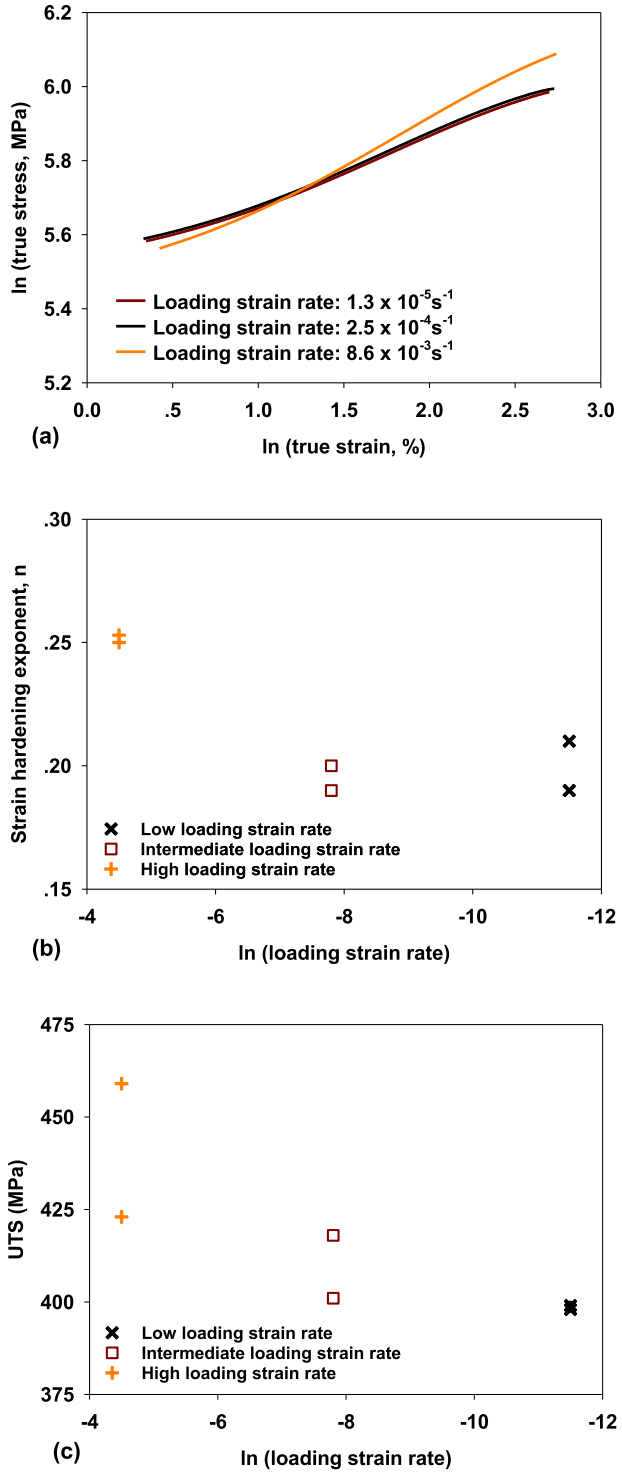

Fig. 9. (a) Natural logarithm (ln) true stress versus ln true strain plots for the strain hardening region at different applied strain rates; plots of (b) strain hardening exponent and (c) UTS with respect to different ln strain rates.

Fig. 6d shows the true stress with respect to the true strain of the compression tests. The data a few seconds prior to facture were not obtained due to the poor quality of DIC images. Fig. 6a–c demonstrate that the true fracture strains were decreased with increasing of initial stress triaxiality. The 0.2% proof stress, ultimate tensile stress (UTS) and final radius of specimens as well as equivalent strain to fracture for each test were summarised in Table 3. The compression specimens buckled and therefore did not fracture. Hence, it was not possible to obtain ultimate tensile stress (UTS) and equivalent strain to fracture for these two compression tests ID7-8.

Fig. 7 shows the plot of 0.2% proof stress versus stress triaxiality. It is evident that the 0.2% proof stress increases steadily with increasing stress triaxiality; an average 14% increase (286 to 325 MPa) from the 0.33 to 0.45 stress triaxiality region and a further 19% increase from the stress triaxiality of 0.45 to 0.7 (325 to 386 MPa).

4.2. Tests under different strain rate

Fig. 8a and b and c and d show two sets of force versus engineering strain and true stress versus strain plots for uniaxial tensile tests of smooth round bar performed under different loading rates. The dark red, black and orange lines present results under applied strain rates of 1.3×10^{-5} s^{-1}, 2.5×10^{-4} $s^{-1}$and 8.6×10^{-3} s^{-1}, respectively. No considerable and consistent changes in the yield stress and elongation can be observed. Fig. 8c and d show that the true stress versus strain curves started to diverge manifestly beyond the yielding point under the applied highest strain rate of 8.6×10^{-3} s^{-1}. This indicates that the plastic flow of CuCrZr alloy is more sensitive to the loading strain rate beyond the yield point. Fig. 9a shows the natural logarithmic true stress and true strain plots in the range of the 0.2% proof stress to the UTS for the fist set of tests. The gradients of the plots represent strain hardening exponents (n) which can be obtained by linearly fitting the plots. Fig. 9b shows the strain hardening exponents, n, as a function of loading strain rates. The strain hardening exponent increased significantly from ~0.2 to 0.25 with increasing loading strain rate from 2.5×10^{-4} s^{-1} to 8.6×10^{-3} s^{-1}. The values of n represent the resistance ability of the CuCrZr alloy to plastic deformation. The dislocation pile-ups might be more significant under applied higher strain rates, which allow the materials to gain higher flow stress. Hence, a ~8% higher UTS was observed in CuCrZr alloy with increased values of n, as shown in Fig. 9b and c. The results obtained from the current study are in a good agreement to those previously observed in a CuCrZr-Ti alloy [20].

4.3. Fracture surface

Figs. 10 and 11 show the SEM images representing the fracture surface features of tested CuCrZr specimens in tension with different stress triaxialities (0.33, 0.45 and 0.69) and under different applied strain rates of 1.3×10^{-5} s^{-1}, 2.5×10^{-4} s^{-1} and 8.6×10^{-3} s^{-1}. The labels 1, 2 and 3 represent SEM images with relatively low, medium and high magnifications. The low magnification images in Figs. 10 and 11 show that for all the cases, the fracture surface morphology includes a ductile zone at the central region and shear lips at the edge. Higher magnification SEM images in Fig. 12a and b show that the central region is decorated by typical ductile equiaxial dimples and voids while the shear lips at the edge showed parabolic elongated dimples. The equiaxed and elongated dimples were formed by a process of voids growth and coalescence due to tensile and shear stresses respectively. Clear dimple walls and slip bands are also shown in Fig. 12b. These slip bands represent dislocation pile-ups due to shear stresses at microscopic scale. The transition from the tensile to shear fracture caused a typical cup-cone shaped fracture morphology. This was consistent across all of the stress triaxiality and strain rate tests conducted in this study.

Fig. 13d–f show the corresponding micro-void mapping of fractured surfaces (Fig. 13a–c) acquired from the central ductile zone of specimens tested specimens at applied low, intermediate and high loading up strain rates respectively. Four different SEM images covering a total characterised area of $400\mu m^2$ were analysed

Table 3
Comparison of 0.2% proof stress, ultimate tensile stress (UTS) and equivalent strain to fracture obtained from the tensile and compression tests.

Test ID	Study		$\sigma_{0.2}$ (MPa)	UTS (MPa)	Final radius (mm)	Equivalent strain to fracture
1	Stress triaxiality	0.33	290	987	1.1	1.99
2	effect	0.33	282	728	1.2	1.75
3		0.45	331	727	1.65	1.20
4		0.45	320	709	1.665	1.18
5		0.69	392	712	1.95	0.86
6		0.69	376	703	1.965	0.85
7		−0.2	302	/	/	/
8		−0.2	296	/	/	/
9	Loading strain	1.3×10^{-5} s^{-1}	208	399	1.11	1.98
10	rate effect		200	398	1.12	1.97
11		2.5×10^{-4} s^{-1}	231	401	1	2.19
12			236	418	1.08	2.04
13		8.6×10^{-3} s^{-1}	226	459	1.02	2.15
14			201	423	1.03	2.14

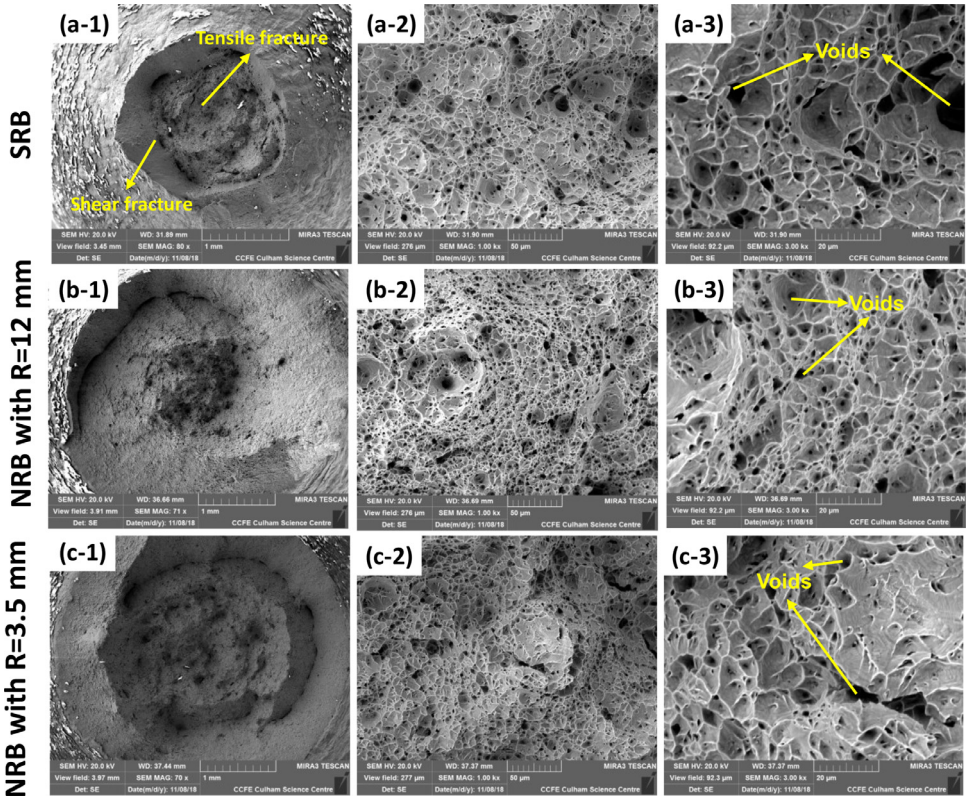

Fig. 10. SEM tensile fractography of (a) smooth round bar sample, (b) notched round bar sample with $R = 3.5$ mm and (c) notched round bar sample with $R = 12$ mm. The 1, 2 and 3 in captions represent relatively low, medium and high magnifications respectively.

Table 4
Summary of quantitative analysis of voids under different strain rates.

Test ID	Strain rate (s^{-1})	Analysis area μm^2	Average void number density (mm^{-2})
9	1.3×10^{-5}	400 μm^2	180 ± 50
11	2.5×10^{-4}	400 μm^2	460 ± 30
13	8.6×10^{-3}	400 μm^2	440 ± 40

for each loading strain rate condition. Table 4 summarises the average nucleated void number density at the centre ductile zone of the specimens tested under different applied strain rates. It can be seen that the number density of void characterised on the fracture surface of specimen tested at loading strain rate of 1.3×10^{-5} s^{-1} is two times less than that of the specimens tested at higher strain rates of 2.5×10^{-4} s^{-1} and 8.6×10^{-3} s^{-1}. The increase of strain rate from 2.5×10^{-4} s^{-1} to 8.6×10^{-3} s^{-1}has no significant influence on the nucleation of voids.

5. Discussion

The relationship between initial stress triaxiality, applied strain rate and equivalent strain to fracture of the CuCrZr specimens

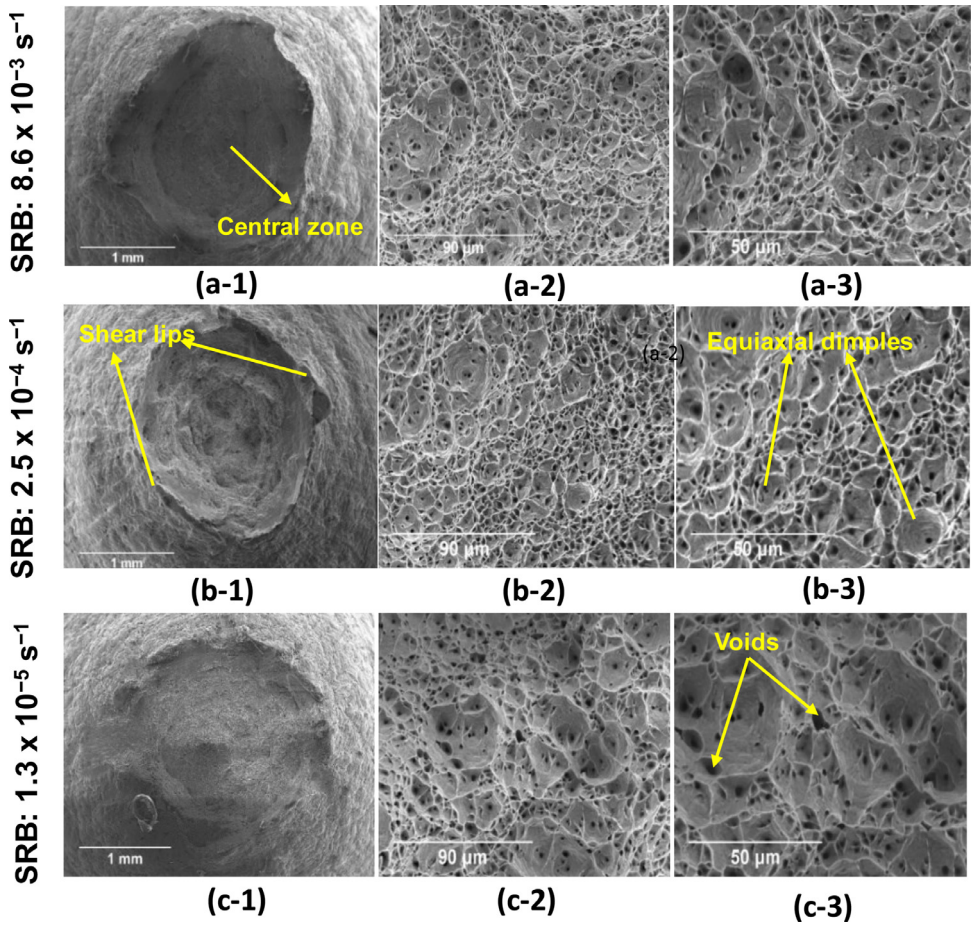

Fig. 11. SEM tensile fractography of smooth round bar sample tested (a) high strain rate 8.6 × 10^{-3} s^{-1}, (b) intermediate strain rate 2.5 × 10^{-4} s^{-1} and (1) low strain rate 1.3 × 10^{-5} s^{-1}. The 1, 2 and 3 in captions represent relatively low, medium and high magnifications respectively.

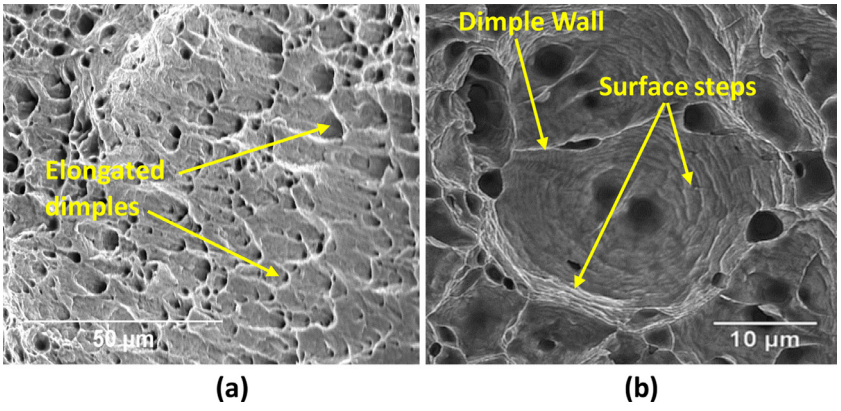

Fig. 12. High magnification SEM images show (a) elongated dimples and (b) an equiaxial dimple showing finer details of dimple wall. Both images taken from test ID9.

tested at room temperature is shown in Fig. 14. The equivalent fracture strain of tensile specimens decreased approximately 60% from ~2.0 to ~0.82 with increased initial stress triaxiality from ~0.33 to 0.7. This agrees with the trend found in typical ductile metals [9,11,21]. The ductility of CuCrZr shows no distinctive change when the loading strain rate was increased from 1.3 × 10^{-5} s^{-1} to 8.6 × 10^{-3} s^{-1}. Overall, this study identifies that the reduction of ductility in CuCrZr at room temperature is dominated by the stress triaxiality effect, but not the loading strain rates.

Furthermore, the relationship between the fracture strain and initial stress triaxiality is fitted by a modified Rice and Tracey exponential equation [9,28].

$$\bar{\varepsilon}_f = 26.1\, exp(-9.45\eta) + 0.82 \quad (8)$$

The fitted curve is shown in Fig. 14 with a solid black line. A satisfied fit was obtained for the current range of stress triaxiality from ~0.33 to 0.7.

An increase in strength often causes a reduction in ductility, which is referred as the strength-ductility trade-off [30]. Although approximately 8% higher UTS was observed in CuCrZr alloy when the loading strain rate was increased from 2.5 × 10^{-4} s^{-1} to 8.6 × 10^{-3} s^{-1}, no significant changes on the ductility was found. This is possibly due to the adiabatic heating effect, which can

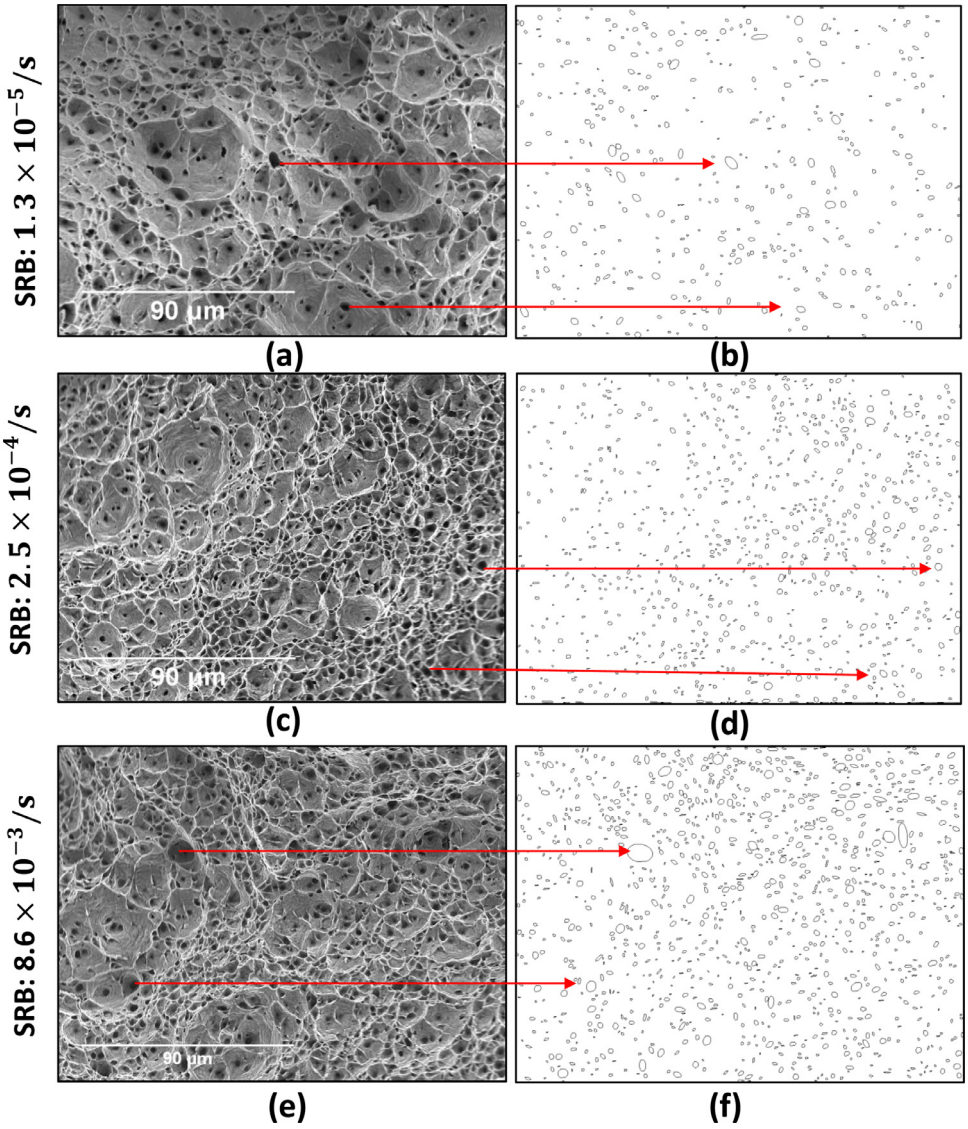

Fig. 13. (b, d and f) Void mapping of representative (a, b and c) SEM images captured from the central zone of the fracture surfaces from tests have been conducted under (a-b) low strain rate, (c-d) intermediate strain rate and (e-f) high strain rate.

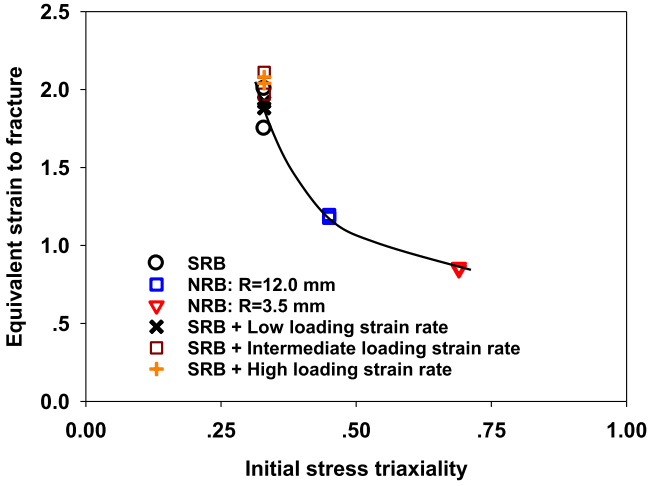

Fig. 14. Plot of equivalent strain fracture versus initial stress triaxiality in CuCrZr.

soften the material and allow dislocations ease more easily during plastic deformation at the applied highest strain rate [31]. The fracture characteristics of the CuCrCr alloy did not alter under different stress triaxialities and applied loading strain rates. For all tests, the ductile failure mechanism is dominated by micro-void nucleation, growth and coalescence. The true stress-strain plots in Fig. 4 show that the maximum principal stresses are reached at lower true strains at higher stress triaxialities of 0.45 and 0.6. This indicates that micro-crack propagation occurs at lower true strains as beyond the UTS the specimens start necking. The combination of micro-crack propagation at lower strains as well as the increase in the void growth and coalescence rates in notched specimens caused the reduction of ductility [9,32–34].

The image processing analysis shows both the average number density and void size are strongly dependant on the stress triaxiality and the loading strain rate. The number density of void increases significantly when the stress triaxiality is increased or the loading strain rate is increased from 1.3×10^{-5} s^{-1} to 2.5×10^{-4} s^{-1}. A possible mechanism that could increase sites for voids nucleation is dislocation 'annihilation' [35] as the in-

crease of loading strain rate creates more dislocation pile-ups. The size/number density of dimples are observed to decrease/increase with increasing in loading strain rates. The dimple size can be affected by the number density of micro- void nucleation sites. When there are fewer and widely spaced voids, the voids have more chance to grow, producing larger dimples. On the contrary, smaller dimples are the indicators of fewer and more closely packed nucleation sites. Voids can coalesce before they have a chance to grow, producing many more small dimples [36]. Figs. 10 and 11 show that the fracture surfaces of NRB specimens were covered with a larger number density of dimples (but with smaller size) than that of in smooth SRB specimens. For given a constant loading strain rate, better ductility represents larger fracture strain and a longer duration of deformation. Hence the microvoids in SRB specimens have a longer time to grow and accumulate to larger dimples than that in NRB specimens. The number density of voids and size of dimples can be also dependant on other factors including impurity of elements and nano-sized precipitates, which were not examined in this study.

6. Conclusions

In this study, the effects of stress triaxiality and applied strain rate on tensile fracture characteristics of a CuCrZr alloy at both macroscopic and microscopic scales were investigated using combined digital-imaging-correlation and electron microscopic techniques. It was found that:

- Optimised strength properties can be achieved in CuCrZr alloys using a brazing process, but care needs to be taken to obtain uniform properties for fusion components of large dimensions.
- The facture ductility of the CuCrZr alloy was found to be strongly dependant on the stress triaxiality. An increase in the initial stress triaxiality from ~0.33 to 0.7 results in a significant decrease in fracture strain.
- Changing the applied strain rate from 1.3×10^{-5} s−1 to 8.6×10^{-3} s−1 has no considerable effect on the ductility of the CuCrZr alloy, but it does result in an increased strain hardening.
- Fracture surface analysis suggested that the fracture mode was ductile for all the monotonic tensile tests. A possible dependency on the void number density, and the sizes of dimples with different stress triaxialities and applied loading strain rates were found.

Future experimental studies on a wider range of stress triaxiality, under higher applied strain rates, and combining the effects of strain rate and stress triaxiality at both room and elevated temperatures are needed to fully understand and quantify their effects on the ductility of CuCrZr alloy. Neutron irradiation has been found can degrade the ductility of this alloy [37]. Hence, an additional set of tests must be performed on irradiated CuCrZr samples.

Declaration of Competing Interest

The authors declare that they have no known competing financial interests or personal relationships that could have appeared to influence the work reported in this paper.

Acknowledgements

This Work has been carried out within the framework of the EUROfusion Consortium and has received funding from the Euratom Research and Training Programme 2014 - 2018 and 2019 - 2020 under grant agreement No 633053. The views and options expressed herein do not necessarily reflect those of the European Commission. Mr Mohamed, Miss Dunn and Dr Sui acknowledge the support from the MicroStructural Studies Unit (MSSU) and Mechanical Testing Facility laboratories at University of Surrey. Dr Wang and Dr Gorley would also like to acknowledge the EPSRC grant EP/T012250/1.

References

[1] M. Lipa, A. Durocher, R. Tivey, T. Huber, B. Schedler, J. Weigert, The use of copper alloy CuCrZr as a structural material for actively cooled plasma facing and in vessel components, Fusion Eng. Des. 75 (2005) 469–473.
[2] M. Gorley, Critical assessment 12: prospects for reduced activation steel for fusion plant, Mater. Sci. Technol. 31 (8) (2015) 975–980.
[3] J.H. You, E. Visca, T. Barrett, B. Böswirth, F. Crescenzi, F. Domptail, M. Fursdon, European divertor target concepts for DEMO: design rationales and high heat flux performance, Nuclear Mater. Energy 16 (2018) 1–11.
[4] D. Marzullo, C. Bachmann, D. Coccorese, Di Gironimo, P. Frosi, G. Mazzone, J.H. You, Progress in the pre-conceptual CAD engineering of European DEMO divertor cassette, Fusion Eng. Des. 146 (2019) 942–945.
[5] M. Fursdon, M. Li, J.H. You, Enhancements in the structural integrity assessment of plasma facing components, Fusion Eng. Des. 146 (2019) 1591–1595.
[6] E. Surrey, Engineering challenges for accelerated fusion demonstrators, Philos. Trans. R. Soc. A 377 (2141) (2019) 20170442.
[7] Z. Kuo, E. Gaganidze, M. Gorley, Development of the material property handbook and database of CuCrZr, Fusion Eng. Des. 144 (2019) 148–153.
[8] P.W. Bridgman, Studies in Large Plastic Flow and Fracture, 177, McGraw-Hill, New York, 1952.
[9] J.R. Rice, D.M. Tracey, "On the ductile enlargement of voids in triaxial stress fields⁎, J. Mech. Phys. Solids 17 (3) (1969) 201–217.
[10] G.R. Johnson, W.H. Cook, "Fracture charatersiatcs of three metals subjected to various strains, strain rates, temperatures and pressures, Eng. Fract. Mech. 21 (1) (1985) 31–48.
[11] M.S. Mirsa, D.C. Barton, The effect of stress triaxiality and strain-rate on the fracture characteristics of ductile metals, J. Mater. Sci. 31 (1996) 453–461.
[12] Y. Bao, T. Wierzbicki, On fracture locus in the equivalent strain and stress triaxiality space, Int. J. Mech. Sci. 46 (1) (2004) 81–98.
[13] Y. Bao, "Dependence of ductile crack formation in tensile tests on stress triaxiality, stress and strain ratios, Eng. Fract. Mech. 72 (4) (2005) 505–522.
[14] C. Tekoğlu, J.W. Hutchinson, T. Pardoen, "On localization and void coalescence as a precursor to ductile fracture, Philos. Trans. R. Soc. A 373 (2038) (2015) 20140121.
[15] P.J. Noell, J.D. Carroll, B.L. Boyce, "The mechanisms of ductile rupture, Acta Mater. 161 (2018) 83–98.
[16] B.P. Croom, H. Jin, P.J. Noell, B.L. Boyce, X. Li., Collaborative ductile rupture mechanisms of high-purity copper identified by in situ X-ray computed tomography, Acta Mater. 181 (2019) 377–384.
[17] G. Trattnig, T. Antretter, R. Pippan, "Fracture of austenitic steel subject to a wide range of stress triaxiality ratios and crack deformation modes, Eng. Fract. Mech. 75 (2) (2008) 223–235.
[18] R. Armstrong, and S. Walley. "High strain rate properties of metals and alloys." 53(3), (2008): pp. 105–128.
[19] J. Wang, W. Guo, J. Guo, Z. Wang, S. Lu., The effects of stress triaxiality, temperature and strain rate on the fracture charateristics of a nickel-base superalloy, J. Mater. Eng. Perform. 25 (5) (2016) 2043–2052.
[20] G.S. Rao, V.M.J. Sharma, S. Ganesh Sundara Raman, M. Amruth, P. Ramesh Narayanan, S.C. Sharma, P.V. VenkitaKrishnan, Effects of temperature and strain rate on tensile properties of Cu-Cr-Zr-Ti Alloy, Mater. Sci. Eng. A 668 (2016) 97–104.
[21] D.C. Barton, Determination of the high strain rate fracture properties of ductile materials using a combined experimental/numerical approach, Int. J. Impact Eng. 30 (8–9) (2004) 1147–1159.
[22] B. Wang, X. Xiao, V.P. Astakhov, Z. Liu, The effects of stress triaxiality and strain rate on the fracture strain of Ti6Al4V, Eng. Fract. Mech. 219 (2019) 106627.
[23] B. Wang, X. Xiao, V.P. Astakhov, Z. Liu, A quantitative analysis of the transition of fracture mechanisms of Ti6Al4V over a wide range of stress triaxiality and strain rate, Eng. Fract. Mech. (2020) 107020.
[24] B.N. Singh, D. Edwards, D., S. Tähtinen, "Effect of heat treatments on precipitate microstructure and mechanical properties of CuCrZr alloy, Forskningscenter Risoe: Technical University of Denmark, 2004.
[25] A. Lukenskas, T.R. Barrett, M. Fursdon, F. Domptail, F. Schoofs, H. Greuner, G. Dose, S. Roccella, E. Visca, F. Gallay, M. Richou, High heat flux test results for a thermal break DEMO divertor target and subsequent design and manufacture development, Fusion Eng. Des. 146 (2019) 1657–1660.
[26] K. Dunn, The effect of heat treatments on the mechanical performance of CuCrZr for fusion reactors, MEng Mechanical Engineering, University of Surrey, 2019.
[27] C.A. Schneider, W.S. Rasband, K.W. Eliceiri, NIH Image to ImageJ: 25 years of image analysis, Nat. Methods 9 (2012) 671–675.
[28] O. Mohamed, The effect of strain rate and stress triaxiality on the mechanical properties of CuCrZr for fusion reactors, BEng Mechanical Engineering, University of Surrey, 2019.
[29] ASTM, E8–99, Standard test methods for tension testing of metallic materialsAnnual Book of ASTM Standards, ASTM, 2001.
[30] Z. Li, K.G. Pradeep, Y. Deng, D. Raabe, C.C. Tasan, Metastable high-entropy dual-phase alloys overcome the strength–ductility trade-off, Nature 534 (7606) (2016) 227–230.

[31] H. Qiu, Integration of temperature, stress state, and strain rate for the ductility of ductile metals, Mater. Trans. 54 (4) (2013) 626–629.
[32] N.H. Kim, C. Oh, Y. Kim, K.B. Yoon, Y.H. Ma., Comparison of fracture strain based ductile failure simulation with experimental results, Int. J. Press. Vessels Pip. 88 (10) (2011) 434–447.
[33] G.R. Johnson, W.H. Cook, A constitutive model and data for metals subjected to large strains, high strain rates and high temperatures, in: Proceedings of the 7th International Symposium on Ballistics, 21, 1983, pp. 541–547.
[34] Z. Li, Y. Zhou, S. Wang, Influence of strain and stress triaxiality on the fracture behavior of GB 35CrMo steel during hot tensile testing, Adv. Mater. Sci. Eng. 2018 (2018).
[35] J.L. González-Velázquez, Fractography and Failure Analysis, 24, Springer International Publishing, 2018.
[36] M. Ohashi, "Extreme value analysis of dimple size on ductile fracture surface associated with fracture behavior of tensile specimens, J. Mater. Sci. (2007) 42.
[37] Y. Ueda, K. Schmid, M. Balden, J.W. Coenen, T. Loewenhoff, A. Ito, A. Hasegawa, C. Hardie, M. Porton, M. Gilbert, Baseline high heat flux and plasma facing materials for fusion, Nucl. Fusion 57 (9) (2017) 092006.